Platinum electrochemistry through a magnifying glass

Jacobse, L.

4 | Voltammetric scanning electrochemical cell microscopy: dynamic imaging of hydrazine oxidation on platinum electrodes

Electrochemical imaging is of interest for visualizing electrochemical processes at interfaces and provides valuable information about the associated kinetics, mass transport and localized activity. Typically, such experiments are performed at constant sample potentials, whereas 'conventional' electrochemical experiments are mostly performed under potentiodynamic conditions. Here, we describe a combination of 'hopping mode' scanning electrochemical cell microscopy (SECCM) and cyclic voltammetry (CV), which enable dynamic imaging with high spatial resolution. Supporting techniques allow for a correlation between local (electrochemical) reactivity of platinum towards hydrazine oxidation and the orientation of the grains in the polycrystalline sample. Furthermore we demonstrate that this reactivity is dramatically influenced by the presence of O_2 under ambient conditions.

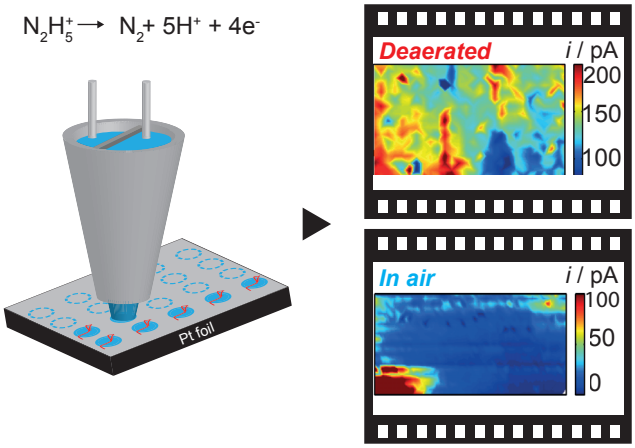

This chapter is based on Chen, C.H., Jacobse, L., McKelvey, K., Lai, S.C.S., Koper, M.T.M., & Unwin, P.R. *Anal. Chem.* **87**, 5782–5789 (2015).

Dynamic electrochemical imaging was first reported by Wipf[1,2] and Schuhmann[3] by combining scanning electrochemical microscopy (SECM) with time-dependent techniques, such as cyclic voltammetry (CV) and potential pulse methods. However, this strategy has not been widely adopted and has also not been used to gain information on heterogeneous electrode surface activity, having employed rather large probe electrodes. Our group has been particularly interested in developing SECCM as a new way to reveal electrode surface activity, as demonstrated by a number of applications.[4–8] Recently, we have adopted a pseudo-single-crystal approach, which combines SECCM and electron backscatter diffraction (EBSD), to study structure–activity relationships at polycrystalline Pt, which comprises high-index Pt facets and grain boundaries.[9,10] However, like other electrochemical imaging approaches[11–13], SECCM has also been limited to imaging experiments at fixed potentials. Using voltammetric SECCM imaging, a full CV is recorded at a number of locations (pixels) on the substrate, which are arranged in a (rectangular) grid. A wealth of information can obtained from these measurements that can then be visualized in different ways (e.g., equipotential maps or spatially resolved CVs).

Here, we focus on spatially resolved studies of the electrocatalytic oxidation of hydrazine on a polycrystalline Pt electrode, and compare these results to those obtained on traditional macro- and microscale electrodes. Hydrazine (N_2H_4) is of practical interest due to its wide application in the fields of electroanalysis and electrocatalysis. Liquid hydrazine is easily transferred and its oxidation offers relatively high power density with carbon-free products, making it a promising fuel for low temperature fuel cells.[14–16] Hydrazine is also important in the pharmaceutical industry, as a common starting material in the synthesis of many pharmaceutical compounds.[17,18] However, it is often a key impurity in pharmaceutical products, and its high toxicity has led to the development of (electrochemical) hydrazine sensors.[19–21] Voltammetric and amperometric hydrazine analysis is usually performed in air, and the role of oxygen in hydrazine detection is rarely taken into account.[22] This is an important consideration, because hydrazine can (catalytically) reduce oxygen on various surfaces, a process that is exploited for corrosion protection.[23–26] Thus, the faradaic response for hydrazine electro-oxidation (especially at trace levels) might be expected to change in the presence of O_2 in a manner that depends on the electrode structure, as we consider herein.

Pt and Pt-based electrodes are relatively active for hydrazine electro-oxidation, and the mechanism and kinetics of hydrazine oxidation on Pt have received ample attention.[27–29] The overall reaction oxidizes hydrazine to molecular nitrogen and depends on the pH of the solution:

$$N_2H_5^+ \longrightarrow N_2 + 5H^+ + 4e^- \qquad \text{(low pH)} \qquad (4.1)$$

$$N_2H_4 + 4OH^- \longrightarrow N_2 + 4H_2O + 4e^- \qquad \text{(high pH)} \qquad (4.2)$$

Various possible intermediates and (pH-dependent) reaction pathways have been proposed. In general, no oxygen-containing compounds are detected by online electrochemical mass spectrometry (OLEMS)[28] and the N–N bond is found to remain intact through isotopic labeling.[30] As this is a catalytic reaction, the role of surface structure is of interest and has been investigated using Pt single crystal electrodes.[31–33] For Pt in a weakly adsorbing electrolyte (perchloric acid), the reactivity (in terms of peak potential) for the basal planes decreases in the order of Pt(100) > Pt(111) > Pt(110).[32] While single-crystal research provides valuable information for basal planes, less is known about high-index surfaces and grain boundaries, of practical importance in polycrystalline or nanoparticle-based sensors.

In this chapter, we use voltammetric SECCM to study hydrazine oxidation at a polycrystalline platinum electrode in air and in a nitrogen atmosphere. Equipotential images and dynamic movies obtained from pixel-resolved CV measurements allow direct visualization of hydrazine oxidation across Pt surfaces at multiple different potentials and surface orientations. In the absence of oxygen, the structure-dependent reactivity of hydrazine oxidation for high-index surfaces is established. In air, the electrochemical current for hydrazine oxidation is found to decrease dramatically for most Pt facets, with important implications for hydrazine electroanalysis.

4.1 Voltammetric SECCM

The setup for voltammetric SECCM is illustrated in Fig. 4.1A. Briefly, a dual barrel pipet with a small opening (in this study ±1 μm diameter) is used to make a series of voltammetric measurements across an area of interest on the Pt sample. The meniscus at the end of the pipet forms an small electrochemical cell at the sample and defines the working electrode area at each pixel. A bias voltage (V_1, in this study 200 mV or 500 mV) is applied between two Pd–H_2 quasi-reference counter electrodes (QRCEs, one in each barrel) to generate an ion conductance current

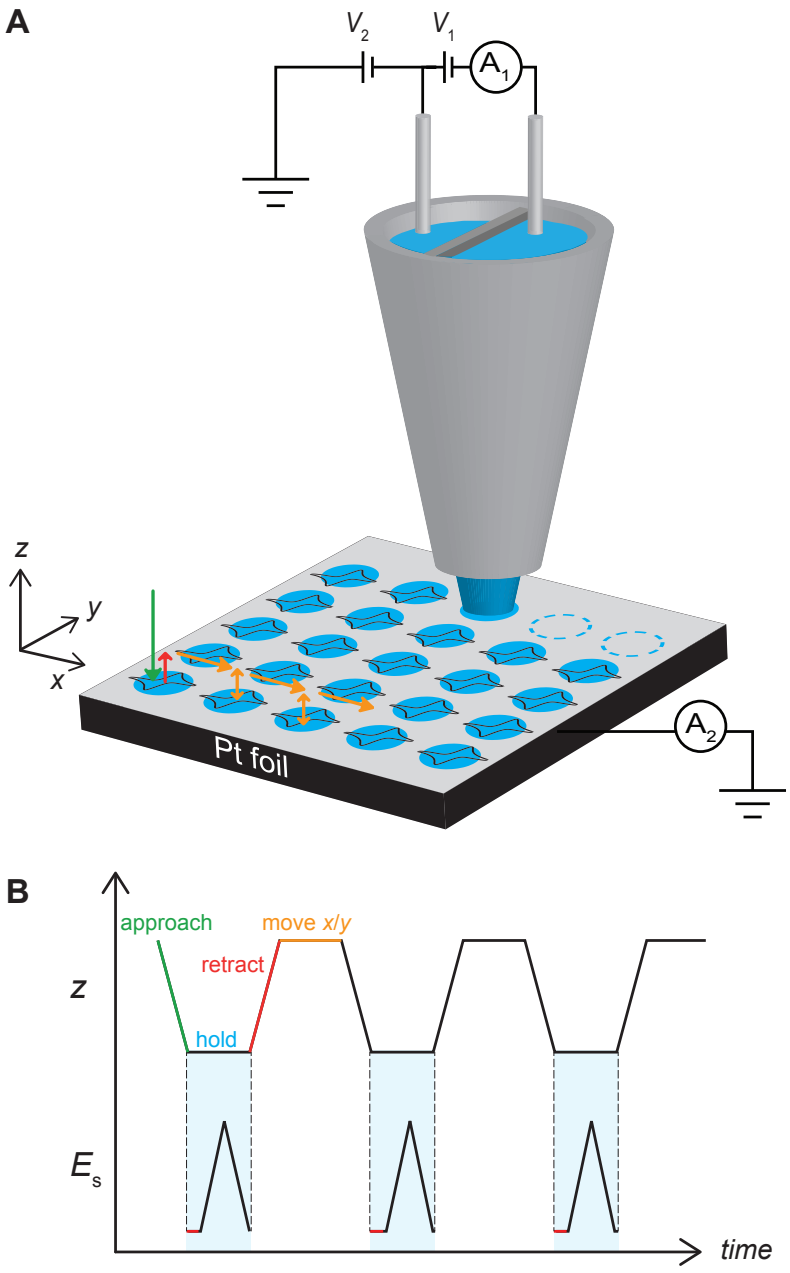

Fig. 4.1 | Hopping mode voltammetric SECCM: (A) Schematic overview of the experimental setup. V_1 and V_2 control the bias and sample voltage. A_1 and A_2 measure the bias and sample current, respectively. The blue circles indicate the probed areas of the sample. The arrows indicate the movement of the pipet. **(B)** Schematic time profiles of the pipet-to-sample separation (top) and the sample potential (bottom).

(i_{DC}) between the barrels across the liquid meniscus. The working electrode potential (E_s) is determined by both V_1 and a voltage (V_2) applied to one of the QRCEs, $E_s = -(V_2 + 0.5 \cdot V_1)$. Modulation of the z-position of the tip (66 or 266 Hz, 25–50 nm peak amplitude) produces an AC component in the ion conductance current (i_{AC}). A constant tip-to-sample distance is maintained by using the magnitude of i_{AC} as input for the feedback.[4–10]

In previous SECCM and related studies, the sample was scanned by the probe using a continuous scanning[10] (for flat substrates) or approach–hold–withdraw (hopping) mode (for rough substrates and/or dissolution studies),[34,35] while the sample, if a conductor, was held at a constant potential (E_s). To obtain potentiodynamic data for a wide potential range in a single experiment, we combine this latter hopping mode SECCM with a potential sweep at each position. As a result, we get a complete, spatially resolved, cyclic voltammogram. Figure 4.1B illustrates the tip-to-sample distance as a function of time during imaging, together with the corresponding applied sample potential. The complete scanning process consists of the following steps: slow approach of the pipet (0.5 $\mu m \cdot s^{-1}$); once in meniscus contact, the pipet position and sample potential are held for 1 s to allow the droplet cell to stabilize; a potential sweep (0.1 $V \cdot s^{-1}$) to obtain the CV was then applied; quick retraction (2.0 $\mu m \cdot s^{-1}$) of the pipet far enough to break the meniscus; and movement in the xy-plane to repeat the process for the next pixel. The retract distance is chosen based on the tip size and the roughness/flatness of the substrate and is typically 1-1.5 μm. For the CV measurement, current data are recorded at least every 1 mV, to produce potentiodynamic movies containing many hundreds of frames. SECCM experiments in deaerated conditions are carried out in an environmental cell, which is placed over the Pt sample and the pipet and is flushed with humidified N_2 (through a vial containing water) before starting the experiment and during imaging.

The resolution of this mode of SECCM imaging is ultimately not determined by the size of pipet apex, but by the distance in between adjacent pixels. This spacing was chosen such (2-3 μm) that there was no overlap between each probed area (diameter ±1 μm). This ensures that a 'fresh' surface (i.e., a region of the surface that has not yet been in contact with the electrolyte solution) is encountered for each pixel, such that all CVs recorded in the SECCM imaging are the first CV at that particular position. Another important factor to determine the pixel spacing is the total imaging time which is typically several hours. Obviously, maintaining

stable and clean imaging conditions at such time scales is challenging. A two-dimensional linear interpolation is applied to the SECCM images in this chapter to guide the eye. We argue that this is reasonable, as in most grains the current was fairly uniform across the grain. More information on the data representation and further experimental details are provided in Appendix E.

4.2 Hydrazine oxidation at Pt electrodes

To study the electrochemistry of hydrazine and provide a comparison for the SECCM results, CV measurements are carried out at polycrystalline platinum electrodes at different length scales. Typical CVs for hydrazine oxidation recorded on a mm-scale platinum wire, on a 25 μm diameter Pt ultramicroelectrode (UME), and on a polycrystalline Pt foil using a 1 μm diameter SECCM pipet are shown in Fig. 4.2. All CVs are recorded in a deaerated solution of 2 mM N_2H_4 in 0.1 M $HClO_4$ at 100 mV·s^{-1}.

At the macroscopic Pt electrode, hydrazine oxidation in an acidic electrolyte starts just after the hydrogen desorption region and then quickly reaches a peak current at ca. 0.48 V. In the case of the UME, (diffusional) mass transport is much faster than that for the macroelectrode. In competition with the surface kinetics for hydrazine electro-oxidation, this leads to an apparent shift in the onset potential to ca. 0.45 V. A steady-state current is observed at potentials above 0.80 V. Similar with CVs reported in literature, hydrazine oxidation is a reasonably facile process at both the macro- and the microscale, leading to mass transport limited reactivity at intermediate overpotentials.[29,36]

Figure 4.2C shows a typical CV for hydrazine oxidation at a platinum foil recorded in the SECCM setup. The oxidation of hydrazine has a similar onset potential as on the UME, but there is a small transient peak in the current at 0.80 V before a quasi-steady state at more anodic potentials. Importantly, Fig. 4.2C shows no features due to oxygen reduction (which would be manifested in observable reduction currents well above the present cathodic onset of ±0.1 V). This confirms the performance of the environmental cell, as the fast diffusion of O_2 from the surroundings across the meniscus to the surface would lead to a noticeable current.[10] Furthermore, as we will show below, the presence of oxygen leads to significantly distorted features in the voltammetric profile for the oxidation of hydrazine. The diffusion coefficient (D)* calculated from the UME experiments

* $i_{lim} = 4nFDcr$,[37] where n is the number of electrons transferred per hydrazine molecule (n = 4), F is the Faraday constant, c is the bulk hydrazine concentration, and r is the UME radius.

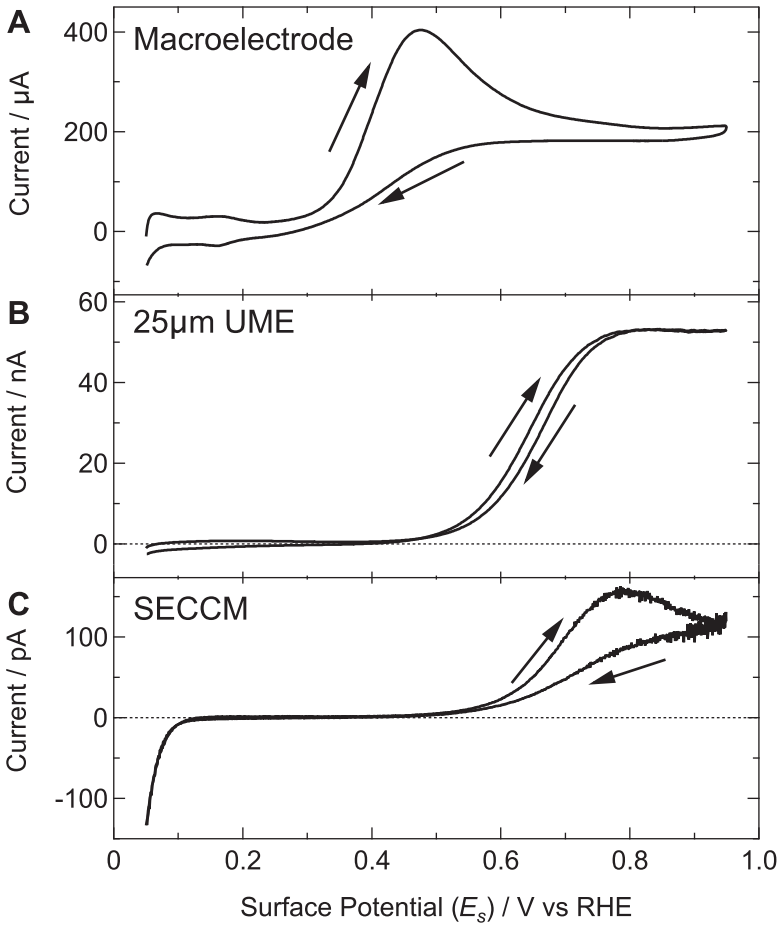

Fig. 4.2 | Hydrazine oxidation at Pt electrodes: Typical CVs of hydrazine oxidation at **(A)** a Pt wire, **(B)** a 25 µm diameter Pt UME, and **(C)** a polycrystalline Pt foil in a SECCM setup. Note the different current scales. In all cases the CVs are recorded in deaerated electrolyte solutions containing 2 mM N_2H_4 in 0.1 M $HClO_4$. The sweep rates are 100 mV·s^{-1}.

is $1.4{\cdot}10^{-5}$ $cm^2{\cdot}s^{-1}$ and is consistent with values reported in the literature.[38,39] In SECCM, the steady-state diffusion-limited current, i_{lim}, beyond the peak is 100 pA. The calculated mean mass transport coefficient, kt ($kt = i_{lim}/nFAc$, where A is the meniscus footprint area), in SECCM is $1.65{\cdot}10^{-2}$ $cm{\cdot}s^{-1}$. This is about 5% of that for an inlaid disk UME ($kt = 4D/\pi r$) of the same size, which is within the typical range reported for a micrometer-sized SECCM pipet,[6] and similar to that of the 25 μm diameter UME. That the SECCM voltammogram shows a slight transient response compared to the UME (cf. Fig. 4.2B and C) is because of the very different current distribution in SECCM with respect to a bulk solution. For $N_2H_5^+$, which is the predominant species herein, there is a large difference in mass transport rate down the two channels of the theta pipet in SECCM.[6] Further, note that some of the differences between the CVs in Fig. 4.2 will be due to the different electrodes used, and methods of preparation, because, as we show herein, hydrazine oxidation is very surface sensitive.

In recent work, a significant 'activation' of a Pt UME after scanning toward high oxidative potentials was reported. This 'activation' was attributed to the formation of catalytically active residual surface oxides in sequential voltammetric scans.[36] Several SECCM CVs were recorded in this study where the potential was scanned up to 1.45 V (see Appendix E). While there are small changes in the voltammetric signature, the responses were generally similar to the 'stabilized' CV reported[36] without the need for any initial activating scan. It should be kept in mind, however, that our surface preparation is an oxidative process (flame-annealing), which could introduce such residual oxides. Nonetheless, to avoid possible complications due to the (more extensive) formation and reduction of Pt oxides, all the CVs in SECCM imaging experiments are recorded from 0.05 to 0.95 V, focusing on the main response.

4.3 Voltammetric SECCM imaging

Figure 4.3A shows an EBSD image of a typical probed area of polycrystalline platinum foil. This plot shows the grain orientation of the sample in the 41x86 μm^2 area (with a pixel spacing of 3 μm) of which the electrochemical activity is imaged in the SECCM experiments.* We will focus on the voltammetry of the four numbered grains as they present the limiting cases of the orientations present. EBSD

* At first sight, this resolution of 14x29 pixels might seem rather low. However, one should realize that, by scanning the potential in such a wide range, the total imaging imaging time already adds up to ~3 hours.

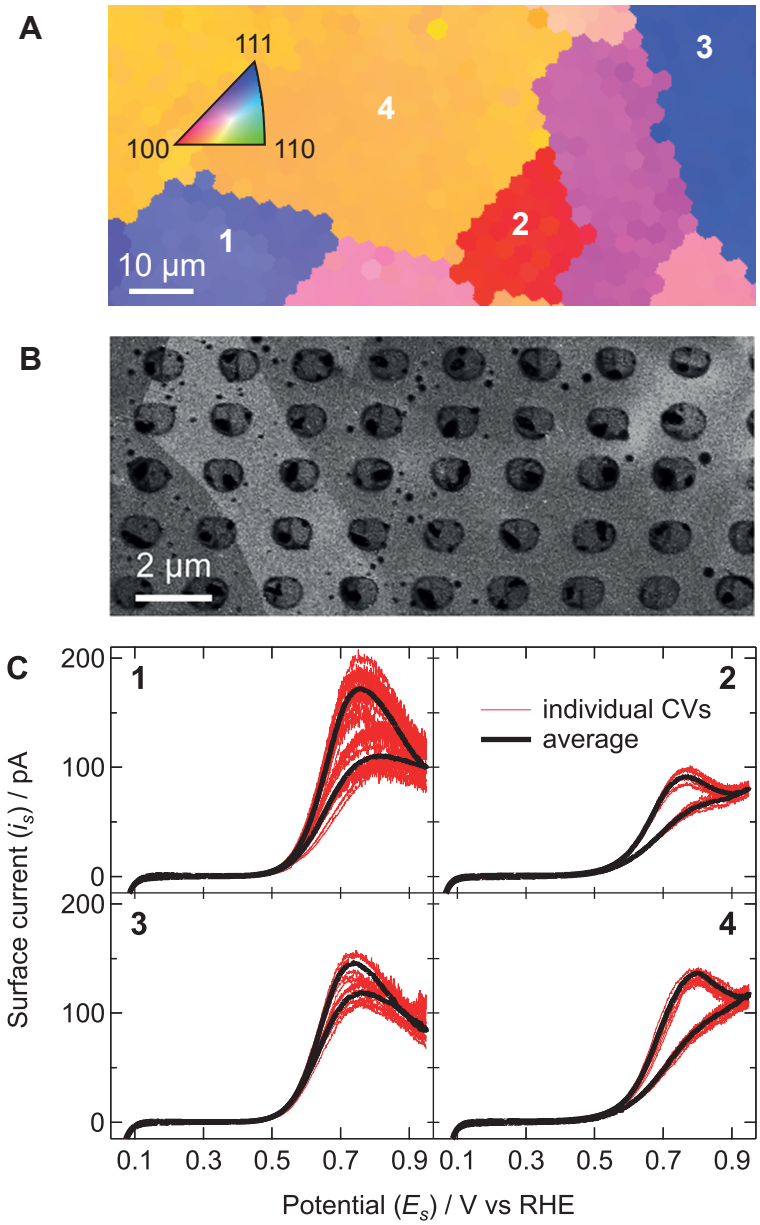

Fig. 4.3 | Structure-activity relationships: **(A)** EBSD image of the Pt foil used in the SECCM imaging experiments. The grain orientations are indicated in the triangle. **(B)** A typical SEM image of a part of a scanned area after SECCM imaging, showing the electrolyte residues on the sample. **(C)** Individual CVs (red, 7–10 for each grain) and grain-averaged CVs (black) for the number grains in (A).

results show that all the grains are high-index surfaces, but grain 1 and 3 have orientations approaching {111}, while grain 2 has an orientation approaching {100}. Grain 4 lies in between {100} and {110}.

Optical microscopy and SEM images after SECCM imaging show droplet residues on the surface due to the quick breaking of the meniscus during probe retraction. Figure 4.3B is a typical zoomed-in SEM image after an SECCM measurement. These droplet residues are fairly consistent in shape and size at the different grains, confirming the stability and reproducibility of the technique and the absence of a significant dependence of droplet wetting on the grain orientation. Additionally, the residues help to determine the exact imaged area and droplet size (meniscus footprint) after SECCM imaging (see also Appendix E).

By combining the results from SECCM, SEM, and EBSD, the position of each individual CV can be determined. Figure 4.3C shows CVs from 7 to 10 pixels obtained on each of the four numbered grains. On top of the individual CVs, an averaged CV is plotted for each grain to show the representative CV feature of that area. It is clear that the variation within a particular grain is fairly small, particularly for grain 2 and grain 4, but the orientation of the grain has a significant impact on its voltammetric response. This is not due to changes in the meniscus contact area as the footprint is reasonably consistent, as pointed out above, and also shown over a more extensive region in Appendix E. Moreover, also the ion conductance current (see Ref. [40]), which is sensitive to the electrochemical footprint shows no structural dependent features. Although all the grains are high-index surfaces, grains 1 and 3, which have contributions mainly from the {111} orientation, have very similar CVs. Grains 2 and 4, which are mainly {100} oriented, show lower peak currents and higher peak potentials. Furthermore, closer inspection reveals that, on grains 1 and 3, the current after the peak decreases reversibly (increasing again after reversal of the potential sweep direction). This is likely related to the initial stages of surface oxide formation on Pt(111) in perchloric acid, which is highly reversible.[41] In contrast, on grains 2 and 4 (mainly {100} orientation), the current continues to decrease after reversal of the sweep direction, mirroring the irreversibility of surface oxidation on Pt(100).[41] Thus, we believe surface oxidation/reduction kinetics is (one of) the factor(s) determining the shape of the voltammogram. Significantly, this effect would have remained unnoticed in (conventional) fixed-potential imaging, highlighting the considerable strength of voltammetric SECCM. Importantly, these results illustrate that hydrazine oxidation at high-index Pt surfaces is strongly structure dependent.

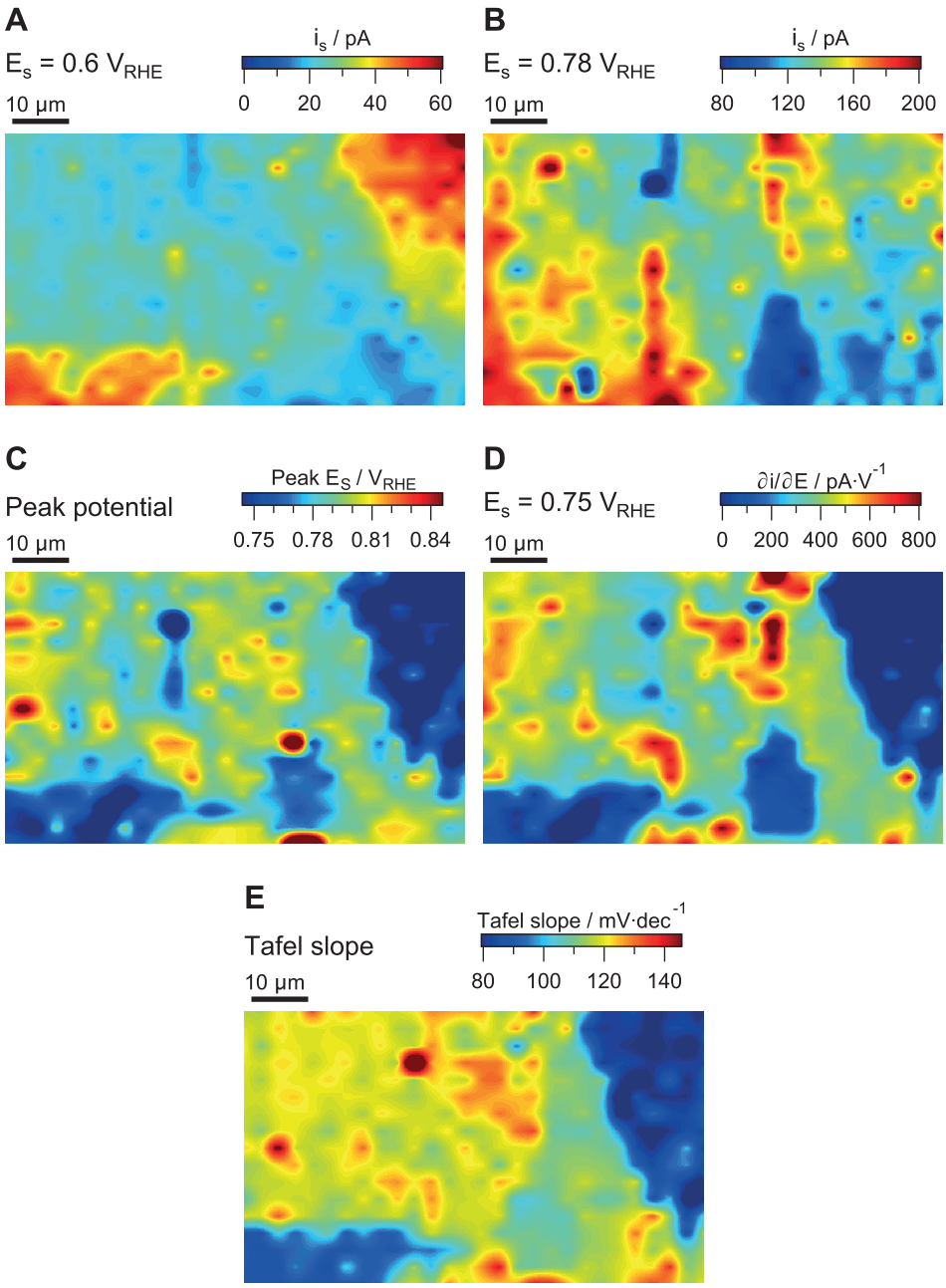

Fig. 4.4 | Maps of SECCM data: Various representations of the SECCM data of a single region; **(A–B)** activity, expressed as substrate current maps for E_s=0.60 and 0.78 V; **(C)** peak potential; **(D)** $\partial i/\partial Es$ at E_s=0.75 V. Note the different color scales. **(E)** Tafel slope in mV per decade determined using the data from $0.45 > E_s > 0.65$ V.

In addition to individual and averaged CVs, the spatially resolved reactivity can be visualized through various types of activity maps. For example, as current values were recorded at least every 1 mV during the pixel-resolved CV measurements, we can construct a series of equipotential maps by plotting the sample current (i_s) of all pixels at a given potential as a function of spatial position. The full series can then be compiled as a movie as shown in Ref. [40], which illustrates the localized evolution of the surface current during a cyclic potential sweep. In the movie, with increasing potential, the activity of different grains starts to show up, providing a direct view of the electrochemical activity across the surface. Figure 4.4A and 4.4B are two frames of data from the i_s movie during the forward scan at potentials of 0.60 and 0.78 V respectively. In these figures, the color scales are adjusted to highlight the full current range at each potential. Such equipotential maps are conceptually similar to maps which could have been obtained with fixed potential SECCM imaging, but with our approach these are only 2 maps out of the 1800 maps that can be constructed from the data at different potentials. The chosen potentials for Fig. 4.4A and 4.4B are close to the onset of the oxidation current (Fig. 4.4A, E_s=0.60 V) and the peak potential (Fig. 4.4B, E_s=0.78 V). In Fig. 4.4A, grains 1 and 3 can be recognized as having higher activity, while grain 2 is more easily recognized in Fig. 4.4B.

As evident in Fig. 4.3C, SECCM CVs on this time scale typically show a peak during the oxidative potential sweep, and the potential at which this peak occurs is related semiquantitatively to the driving force required for the reaction. This is shown in Fig. 4.4C, from which it is clear that the peak occurs at lower overpotential, the higher the current in the surface activity maps in Fig. 4.4A and 4.4B. Using another approach, a high order polynomial is fitted through each pixel-resolved CV to calculate $\partial i/\partial E_s$, with the result at E_s=0.75 V shown in Fig. 4.4D. This quantity again gives a measure of the ease of reaction, and the result is a map showing the distinct behavior of the different grains. Finally, a Tafel analysis is performed for all four grains, using the potential interval from 0.45 to 0.65 V (at the foot of the wave, where mass transport and concentration polarization can be neglected) and is shown in Fig. 4.4E. For the whole area, the apparent Tafel slope is mainly within the range of 80 to 140 mV per decade. This range is within that of the previously reported Tafel slope values, 82 mV per decade to 110 mV per decade, for polycrystalline Pt electrodes in acidic solution.[29,42] However, our data are showing that the precise slope is very grain-orientation dependent. The average Tafel slopes for grains from 1 to 4 are 100±12, 130±2, 88±3, and 139±3 mV per decade,

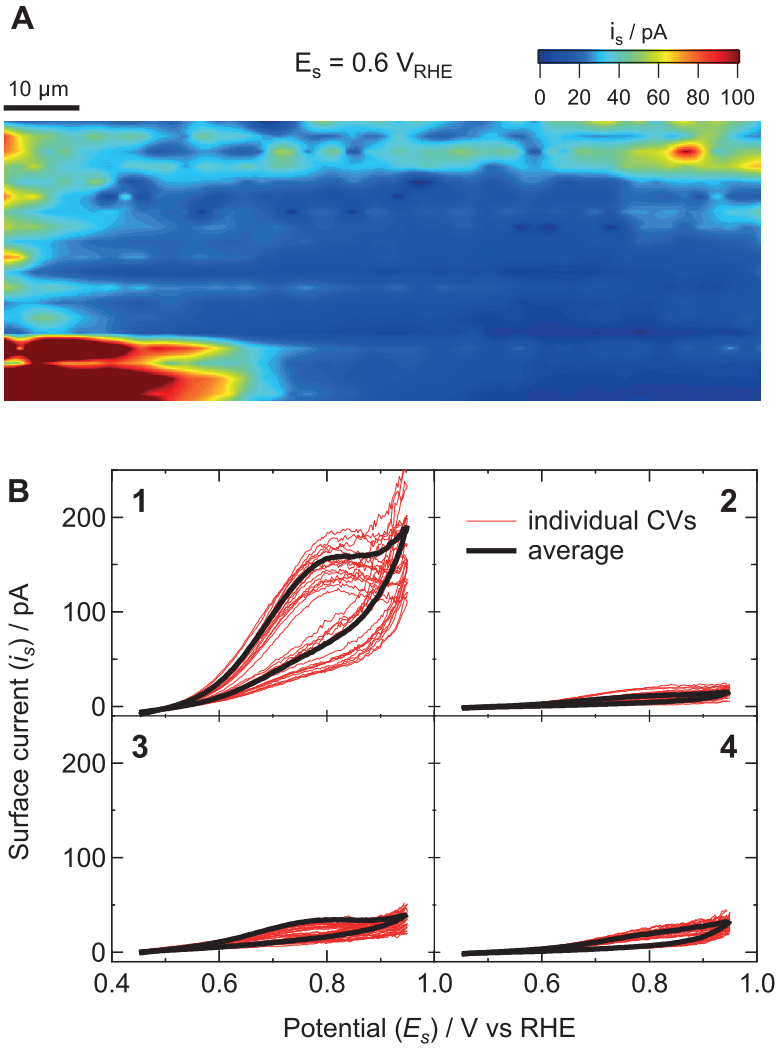

Fig. 4.5 | Hydrazine oxidation in air: (A) Equipotential i_s map of hydrazine oxidation at E_s=0.78 V. **(B)** Individual (red, 10–20 for each grain) and averaged (black) CVs for different grains. Numbers in (B) correspond to grain areas marked in Fig. 4.3a.

respectively. By comparing Fig. 4.4A–B to 4.4C–E, it is demonstrated through the use of voltammetric SECCM that it becomes possible to visualize/identify differences (especially in the $\partial i/\partial Es$ maps) in electrochemical activity which would be invisible using fixed potential imaging.

4.4 Hydrazine oxidation in air

Besides the faradaic oxidation of hydrazine, there are also studies reporting catalytic (nonfaradaic) decomposition of hydrazine.[25,43] Although the nonfaradaic oxidation of hydrazine in air is slow at room temperature, it can be accelerated in the presence of catalysts, such as platinum, copper, and manganese.[25,30,43] Recently, we have demonstrated that the three-phase boundary in SECCM[10] provides high mass transport of oxygen, making SECCM is an interesting technique to study the role of O_2 in the total oxidation reaction. Thus, imaging experiments are performed in the same area as shown in Fig.4.3A, after cleaning the surface, but now without using the environmental cell. CVs are recorded every 2 μm between 0.45 and 0.95 V.

Figure 4.5A shows an equipotential i_s map extracted from the SECCM imaging experiment in air, at 0.78 V. Movies of i_s and i_{DC} for the CV measurements are available in Ref. [40]. Compared to Fig. 4.3C, Fig. 4.5A shows that, except for grain 1, the electrochemical activity of all the grains is almost completely suppressed. Similar to the approach in Fig. 4.3C, CVs recorded at grains 1 to 4 at single pixels (red) and the averaged ones (black) are shown in Fig. 4.5B. It is clear that hydrazine oxidation CVs in air exhibit different shapes and much lower current values compared with CVs in the absence of O_2. Simultaneously, the peak current, when discernible, shifts to higher overpotential.

To further understand the role of oxygen and the cause of the large differences in activity, we perform a blank SECCM experiment in air, using just the supporting electrolyte. The potential is scanned between 0.45 and 1.35 V at a sweep rate of $0.5\ V{\cdot}s^{-1}$. Averaged CVs in each of the four grains for all three imaging experiments (hydrazine oxidation in a deaerated solution, hydrazine oxidation in the presence of dissolved oxygen, and blank CVs) are summarized in Fig. 4.6. By comparing the three measurements, it is clear that, generally, the presence of oxygen leads to a decrease in the currents observed for the oxidation of hydrazine. There are two main causes of this effect.

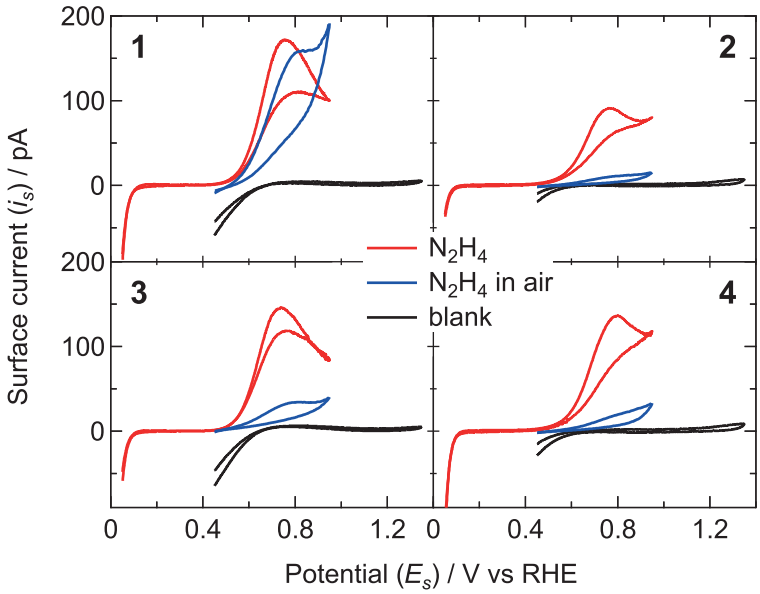

Fig. 4.6 | The effect of air on the oxidation of hydrazine: Comparison of N_2H_4 oxidation (red) in deaerated environment, N_2H_4 oxidation in air (blue), and blank (in air, black) averaged CVs for different grain orientations (numbers indicated).

First, it can be seen in the blank CVs that, at potentials below 0.65 V, there is a significant (reduction) current due to the oxygen reduction reaction (ORR), in agreement with our previous findings.[10] Thus, at potentials between 0.45 and 0.65 V, the oxidation of hydrazine (positive current) overlaps with the reduction of oxygen (negative current) in an aerated solution, and the overall observed current in this potential range represents the sum of the two processes. As a result, the apparent current for the oxidation of hydrazine in air in this potential range is much smaller than that of the oxidation of hydrazine in deaerated conditions (and, similarly, the reduction current of oxygen with hydrazine present is smaller (in absolute terms) than that of the reduction of oxygen in the absence of hydrazine). Second, as mentioned above, hydrazine can react with oxygen through the following reaction at a catalyst (such as platinum) surface:

$$N_2H_4 + O_2 \longrightarrow N_2 + 2H_2O \tag{4.3}$$

This nonfaradaic (i.e., no 'current-producing') reaction consumes hydrazine, thereby lowering the interfacial concentration of hydrazine. In fact, this reaction is most likely exacerbated in our experimental setup, as is the ORR effect mentioned above, due to the enhanced mass transport of oxygen at the three-phase boundary.[10] Consequently, a lower current for the (electrochemical) oxidation of hydrazine is observed compared to a deaerated solution, as the current is directly proportional to the hydrazine concentration.

In fact, we can exploit this second mechanism to obtain the structural dependency (at least in a semiquantitative manner) of the nonfaradaic reaction between oxygen and hydrazine. By using the observed current in the presence of oxygen as a probe for the residual hydrazine concentration (that is, the hydrazine concentration after the nonfaradaic consumption of hydrazine), we can deduce the extent to which the nonfaradaic reaction takes place. Specifically, regions of the sample where there is a small decrease in current (such as grain 1) indicate low activity toward the nonfaradaic reaction, whereas a large decrease (such as grains 2, 3, and 4) represents high activity. Using this approach, we find the activity toward the nonfaradaic reaction of hydrazine and oxygen to follow the following relative order: grain 2 > grain 4 > grain 3 > grain 1. Interestingly, this is the inverse of the electrochemical activity (see Fig. 4.3C), and at least in part, this rationalizes the trend because the faradaic and nonfaradaic processes are in competition. Importantly, these results provide a novel method to probe local structure effects in nonfaradaic catalytic reactions through electrochemical measurements, an avenue we will further explore in the future. There are also clearly implications

for the optimal design of hydrazine voltammetric sensors in an aerated solution.

4.5 Conclusions

In this chapter, we have highlighted the considerable power of voltammetric SECCM, which combines SECCM with CV measurements, as a methodology for electrochemical imaging. Compared to traditional fixed potential imaging,[5,8,10,44] this approach has significant attributes. First, as CVs are recorded at every pixel of the scanned area, it is possible to probe local electrochemical currents at multiple potentials (1800 separate potentials in the deaerated hydrazine CVs herein) and thus increase imaging efficiency. Furthermore, as the meniscus breaks and droplet residues are left on the substrate, as the pipet moves to a new position on the substrate for the next measurement, it is possible to determine the exact position and surface area of each pixel. Finally, it allows for potentiodynamic information to be obtained, complementing potentiostatic information from fixed potential imaging, which both have their uses in certain situations (cf. cyclic voltammetry and chronoamperometry).

In this work, using voltammetric SECCM, we studied hydrazine oxidation at high-index Pt surfaces in air and in a deaerated environment. We found the CV characteristics of hydrazine oxidation at the Pt electrode to be strongly surface structure dependent. The reactivity of hydrazine at different surfaces can be compared from equipotential maps and dynamic movies. For the grain orientations studied here, grains having more {111} features show higher activity than grains having more {100} features. This might appear to counter studies with single-crystal electrodes, but it should be noted that the studies herein are on high-index and high-defect facets, highlighting the importance of such features in the electrocatalytic oxidation of hydrazine oxidation on practical surfaces.

Significant changes in hydrazine oxidation activity were observed in air, where oxygen transfers through the three-phase boundary of the SECCM with high rates. We found the presence of oxygen strongly decreased the detected electrochemical current for hydrazine oxidation at most of the Pt grains. The variation in activity between different grains was also much more pronounced than in the absence of air. We ascribe these changes to the overlap between the potentials for hydrazine oxidation and ORR, as well as to the nonfaradaic decomposition of hydrazine with oxygen at certain Pt facets. These results emphasize the importance of considering oxygen in the voltammetric detection of hydrazine, which could greatly affect the response of hydrazine sensors in a manner dependent on the Pt substrate used.

References

1. Díaz-Ballote, L., Alpuche-Aviles, M. & Wipf, D. O. Fast-scan cyclic voltammetry–scanning electrochemical microscopy. *J. Electroanal. Chem.* **604,** 17–25 (2007).
2. Schrock, D. S., Wipf, D. O. & Baur, J. E. Feedback Effects in Combined Fast-Scan Cyclic Microscopy. *Anal. Chem.* **79,** 4931–4941 (2007).
3. Nebel, M., Grützke, S., Diab, N., Schulte, A. & Schuhmann, W. Microelectrochemical visualization of oxygen consumption of single living cells. *Faraday Discuss.* **164,** 19 (2013).
4. Ebejer, N., Schnippering, M., Colburn, A. W., Edwards, M. A. & Unwin, P. R. Localized high resolution electrochemistry and multifunctional imaging: Scanning electrochemical cell microscopy. *Anal. Chem.* **82,** 9141–9145 (2010).
5. Ebejer, N. *et al.* Scanning Electrochemical Cell Microscopy: A Versatile Technique for Nanoscale Electrochemistry and Functional Imaging. *Annu. Rev. Anal. Chem.* **6,** 329–351 (2013).
6. Snowden, M. E. *et al.* Scanning electrochemical cell microscopy: Theory and experiment for quantitative high resolution spatially-resolved voltammetry and simultaneous ion-conductance measurements. *Anal. Chem.* **84,** 2483–2491 (2012).
7. Lai, S. C. S., Patel, A. N., McKelvey, K. & Unwin, P. R. Definitive evidence for fast electron transfer at pristine basal plane graphite from high-resolution electrochemical imaging. *Angew. Chem. Int. Ed.* **51,** 5405–5408 (2012).
8. Güell, A. G., Ebejer, N., Snowden, M. E., MacPherson, J. V. & Unwin, P. R. Structural correlations in heterogeneous electron transfer at monolayer and multilayer graphene electrodes. *J. Am. Chem. Soc.* **134,** 7258–7261 (2012).
9. Aaronson, B. D. *et al.* Pseudo-single-crystal electrochemistry on polycrystalline electrodes: Visualizing activity at grains and grain boundaries on platinum for the Fe_2^+/Fe_3^+ redox reaction. *J. Am. Chem. Soc.* **135,** 3873–3880 (2013).
10. Chen, C.-H., Meadows, K. E., Cuharuc, A., Lai, S. C. S. & Unwin, P. R. High resolution mapping of oxygen reduction reaction kinetics at polycrystalline platinum electrodes. *Phys. Chem. Chem. Phys.* **16,** 18545 (2014).
11. Bard, A. J. & Faulkner, L. R. *Electrochemical methods : fundamentals and applications* 833 (Wiley, 2001).
12. Bard, A. J., Fan, F. R. F., Kwak, J. & Lev, O. Scanning Electrochemical Microscopy. Introduction and Principles. *Anal. Chem.* **61,** 132–138 (1989).
13. Amemiya, S., Bard, A. J., Fan, F.-R. F., Mirkin, M. V. & Unwin, P. R. Scanning Electrochemical Microscopy. *Annu. Rev. Anal. Chem.* **1,** 95–131 (2008).
14. Serov, A. & Kwak, C. Direct hydrazine fuel cells: A review. *Appl. Catal., B* **98,** 1–9 (2010).
15. Yamada, K. *et al.* Investigation of PEM type direct hydrazine fuel cell. *J. Power Sources* **115,** 236–242 (2003).
16. Rees, N. V. & Compton, R. G. Carbon-free energy: a review of ammonia- and hydrazine-based electrochemical fuel cells. *Energy Environ. Sci.* **4,** 1255 (2011).
17. Elder, D. P., Snodin, D. & Teasdale, A. Control and analysis of hydrazine, hydrazides and hydrazones-Genotoxic impurities in active pharmaceutical ingredients (APIs) and drug products. *J. Pharm. Biomed. Anal.* **54,** 900–910 (2011).
18. Liu, D. Q., Sun, M. & Kord, A. S. Recent advances in trace analysis of pharmaceutical genotoxic impurities. *J. Pharm. Biomed. Anal.* **51,** 999–1014 (2010).
19. Metters, J. P., Tan, F., Kadara, R. O. & Banks, C. E. Platinum screen printed electrodes for the electroanalytical sensing of hydrazine and hydrogen peroxide. *Anal. Methods* **4,** 1272 (2012).
20. Liu, J., Li, Y., Jiang, J. & Huang, X. C@ZnO nanorod array-based hydrazine electrochemical sensor with improved sensitivity and stability. *Dalton Trans.* **39,** 8693 (2010).
21. Chakraborty, S. & Raj, C. R. Carbon nanotube supported platinum nanoparticles for the voltammetric sensing of hydrazine. *Sens. Actuators, B* **147,** 222–227 (2010).
22. Hu, G., Zhou, Z., Guo, Y., Hou, H. & Shao, S. Electrospun rhodium nanoparticle-loaded carbon nanofibers for highly selective amperometric sensing of hydrazine. *Electrochem. Commun.* **12,** 422–426 (2010).

23. Moussa, M. N. H., Taha, F. I. M., Gouda, M. M. A. & Singab, G. M. The effect of some hydrazine derivatives on the corrosion of Al in HCl solution. *Corros. Sci.* **16,** 379–385 (1976).
24. Andries, V. & Couturier, D. Reduction of dissolved oxygen in water: Hydrazine and its organic substitutes. *Mater. Performance* **39,** 58–61 (2000).
25. Cuy, E. J. & Bray, W. C. The oxidation of hydrazine. II. The effect of oxygen on the decomposition of hydrazine. The reactions with ferricyanide in alkaline solution, and dichromate in acid solution. *J. Am. Chem. Soc.* **46,** 1786–1795 (1924).
26. Moon, J., Park, K., Kim, J. & Seo, G. The reduction reaction of dissolved oxygen in water by hydrazine over platinum catalyst supported on activated carbon fiber. *Appl. Catal., A* **184,** 41–48 (1999).
27. Bard, A. J. Chronopotentiometric Oxidation of Hydrazine at a Platinum Electrode. *Anal. Chem.* **35,** 1602–1607 (1963).
28. Rosca, V. & Koper, M. T. M. Electrocatalytic oxidation of hydrazine on platinum electrodes in alkaline solutions. *Electrochim. Acta* **53,** 5199–5205 (2008).
29. García, M. D., Marcos, M. L. & Velasco, J. G. On the mechanism of electrooxidation of hydrazine on platinum electrodes in acidic solutions. *Electroanalysis* **8,** 267–273 (1996).
30. Arnolds, K., Heitbaum, J. & Vielstich, W. Investigations on the Rupture of the N-N-Bond within the Anodic Oxidation and Catalytic Decomposition of Hydrazine. *Z. Naturforsch. A: Phys., Phys. Chem., Kosmophys.* **29,** 359–362 (1974).
31. Nishihara, C. *et al.* Behavior of hydrazine and its effects on the adsorption of hydrogen at Pt(322) and Pt(111) electrodes in sulfuric acid solutions. *J. Electroanal. Chem.* **338,** 299–316 (1992).
32. Álvarez-Ruiz, B., Gómez, R., Orts, J. M. & Feliu, J. M. Role of the Metal and Surface Structure in the Electrooxidation of Hydrazine in Acidic Media. *J. Electrochem. Soc.* **149,** D35 (2002).
33. Gómez, R. & Clavilier, J. Electrochemical behaviour of platinum surfaces containing (110) sites and the problem of the third oxidation peak. *J Electroanal Chem* **354,** 189–208 (1993).
34. Kinnear, S. L. *et al.* Dual-barrel conductance micropipet as a new approach to the study of ionic crystal dissolution kinetics. *Langmuir* **29,** 15565–15572 (2013).
35. Edwards, M. A., Williams, C. G., Whitworth, A. L. & Unwin, P. R. Scanning ion conductance microscopy: A model for experimentally realistic conditions and image interpretation. *Anal. Chem.* **81,** 4482–4492 (2009).
36. Aldous, L. & Compton, R. G. The mechanism of hydrazine electro-oxidation revealed by platinum microelectrodes: role of residual oxides. *Phys. Chem. Chem. Phys.* **13,** 5279–5287 (2011).
37. Saito, Y. A Theoretical Study on the Diffusion Current at the Stationary Electrodes of Circular and Narrow Band Types. *Review of Polarography* **15,** 177–187 (1968).
38. Dudin, P. V., Unwin, P. R. & Macpherson, J. V. Electro-oxidation of hydrazine at gold nanoparticle functionalised single walled carbon nanotube network ultramicroelectrodes. *Phys. Chem. Chem. Phys.* **13,** 17146–17152 (2011).
39. Eisner, U. & Gileadi, E. Anodic oxidation of hydrazine and its derivatives. *J. Electroanal. Chem. Interfacial Electrochem.* **28,** 81–92 (1970).
40. Chen, C. H. *et al.* Voltammetric scanning electrochemical cell microscopy: Dynamic imaging of hydrazine electro-oxidation on platinum electrodes. *Anal. Chem.* **87,** 5782–5789 (2015).
41. Rodes, A., Zamakhchari, M., El Achi, K. & Clavilier, J. Electrochemical behaviour of Pt(100) in various acidic media. *J. Electroanal. Chem. Interfacial Electrochem.* **305,** 115–129 (1991).
42. Harrison, J. A. & Khan, Z. A. The oxidation of hydrazine on platinum in acid solution. *J. Electroanal. Chem.* **28,** 131–138 (1970).
43. Gaunt, H. & Wetton, E. A. M. The reaction between hydrazine and oxygen in water. *J. Appl. Chem.* **16,** 171–176 (2007).
44. Lai, S. C. S., Dudin, P. V., MacPherson, J. V. & Unwin, P. R. Visualizing zeptomole (electro)catalysis at single nanoparticles within an ensemble. *J. Am. Chem. Soc.* **133,** 10744–10747 (2011).